Model predictive control for thermal stress-aware power modulation of solid oxide fuel cell systems

de Lange, Matthis H.; Segovia, Pablo; Negenborn, Rudy R.; van Biert, Lindert

DOI
10.1016/j.enconman.2025.120395

Publication date
2026

Document Version
Final published version

Published in
Energy Conversion and Management

Citation (APA)
de Lange, M. H., Segovia, P., Negenborn, R. R., & van Biert, L. (2026). Model predictive control for thermal stress-aware power modulation of solid oxide fuel cell systems. *Energy Conversion and Management*, *347*, Article 120395. https://doi.org/10.1016/j.enconman.2025.120395

Energy Conversion and Management 347 (2026) 120395

Contents lists available at ScienceDirect

Energy Conversion and Management

journal homepage: www.elsevier.com/locate/enconman

Research paper

Model predictive control for thermal stress-aware power modulation of solid oxide fuel cell systems

Matthis H. de Lange [a,*], Pablo Segovia [b,c], Rudy R. Negenborn [a], Lindert van Biert [a]

[a] Maritime & Transport Technology, Delft University of Technology, Mekelweg 5, Delft, 2628 CD, The Netherlands
[b] Department of Automatic Control, Universitat Politècnica de Catalunya - BarcelonaTECH, Av. Diagonal 647, Barcelona, 08028, Spain
[c] Institut de Robòtica i Informàtica Industrial, CSIC-UPC, Carrer de Llorens i Artigas, 4, Barcelona, 08028, Spain

ARTICLE INFO

Keywords:
Solid oxide fuel cells
Maritime energy system
Alternative fuels
Model predictive control
Thermal stress
Dynamic power tracking

ABSTRACT

This paper introduces a model predictive control (MPC) strategy for solid oxide fuel cell (SOFC) systems, introducing thermal stress-aware power modulation. The proposed MPC approach incorporates a temperature rate-of-change constraint to manage local temporal and spatial temperature gradients in the SOFC during transient power modulation. The study evaluates the sensitivity and effectiveness of the temperature rate-of-change constraint under four different constraint parameter sets, spanning a range from fast to slow power modulation. A one-dimensional spatially discretised SOFC model is employed in the simulations to assess the resulting local temperature gradients. The results of this paper indicate that the proposed MPC strategy enhances transient power tracking performance compared to the conventional approach of using an electrical current rate-of-change constraint with 1%–17%, without a significant increase in the local temporal and spatial temperature gradients in the SOFC.

1. Introduction

The maritime sector is moving forward in the energy transition towards a more sustainable future, motivated by its substantial contribution to worldwide emissions and regulations. In 2018, the sector accounted for 2.89% of worldwide emissions [1], a figure projected to increase without immediate mitigating measures. The *International Maritime Organization* (IMO) and the *European Union* (EU) have therefore established regulatory frameworks aiming for 40% *Greenhouse Gas* (GHG) emission reduction by 2030 [2] and 80% GHG emission reduction by 2050 [3], respectively.

Onboard a ship, the power generation system is the main source of GHG and polluting emissions, primarily originating from *Internal Combustion Engines* (ICE) combined with fossil fuels to provide the propulsion and the electricity generation [4]. Renewable fuels, such as hydrogen, methanol, and ammonia, are crucial in reducing GHG and pollutant emissions [4–6]. There is extensive research in making these fuels compatible with ICEs, but after treatment is required to reduce the pollution emissions [7]. Therefore, other types of power generation systems, like fuel cells, are seen as promising to contribute to the energy transition in the maritime sector [8–10]. The *Proton-Exchange Membrane Fuel Cell* (PEMFC) and *Solid Oxide Fuel Cell* (SOFC) can operate with various alternative fuels, potentially improving the electrical efficiency compared to an ICE and reducing the polluting emission [9,11]. Future onboard power generation systems are expected to be a hybrid combination of ICEs, fuel cells, batteries, and electric motors compatible with various alternative fuels [12–14], where the exact configuration will depend on the ship type and mission profile. Batteries are considered practical for ships with short mission profiles, but impractical for ocean-going vessels due to the low energy density [15].

The PEMFC has a relatively high energy density and quick response to load transients. However, PEMFC encounters challenges regarding fuel flexibility, as it needs to operate with pure hydrogen (a purity over ≥99% is required), due to its low operation temperature and material of the *Positive-electrode Electrolyte Negative-electrode* (PEN) structure. This approach requires bringing hydrogen onboard, which demands either large volumetric storage at room temperature or the use of complex and costly systems to store hydrogen in liquefied or pressurised form. Additionally, one could use the PEMFC with other alternative fuels requiring pre-reforming and extensive purification, which increases system complexity and reduces electrical efficiency [16]. In contrast, SOFCs can internally reform certain alternative fuels (e.g., LNG, ammonia, and methanol). This internal reforming capability results in a simplified system with higher efficiency [16,17], making SOFCs well-suited for larger ship types and deep-sea shipping. However, the primary limitation of SOFCs lies in their transient performance. To

* Corresponding author.
E-mail address: m.h.delange@tudelft.nl (M.H. de Lange).

https://doi.org/10.1016/j.enconman.2025.120395
Received 2 June 2025; Received in revised form 1 August 2025; Accepted 15 August 2025
Available online 23 September 2025

Nomenclature

Greek symbols

$\bar{\eta}$	overall efficiency t (–)
χ	mole fraction (–)
Δ	difference operator
η	efficiency (–)
γ	specific heat ratio (–)
λ	heat transfer coefficient ($\mathrm{W\,m^{-2}}$)
μ	utilization (–)
ω	angular velocity ($\mathrm{s^{-1}}$)
ϕ	ratio (–)
Π	power tracking KPI (–)
Σ	system
τ	torque ($\mathrm{N\,m}$)
θ	sample-time variable
ξ	extended state vector

Roman symbols

$\bar{H}$	specific enthalpy ($\mathrm{J\,mol^{-1}}$)
$\bar{R}$	universal gas constant ($\mathrm{J\,mol^{-1}\,K^{-1}}$)
$\mathcal{A}, \mathcal{B}, \mathcal{C}$	system matrices velocity form
$\mathcal{F}$	Faraday constant ($\mathrm{C\,mol^{-1}}$)
$\mathcal{P}$	power (W)
$\mathcal{R}$	ohmic resistance (Ω)
$\dot{n}$	molar flow ($\mathrm{mol\,s^{-1}}$)
$\dot{Q}$	heat flux (W)
$\mathbb{U}$	compact input set
$\mathbb{X}$	compact state set
$\mathbb{Y}$	compact output set
$\mathbb{Z}$	set of integers
A	area ($\mathrm{m^2}$)
a	molar flow coefficient (mol)
C	viscous friction ($\mathrm{kg\,m^2\,s^{-1}}$)
c_p	heat capacity ($\mathrm{J\,mol^{-1}\,K^{-1}}$)
F	discrete-time system dynamics
f	continous-time system dynamics
H	enthalpy (J)
h	output function
I	rotational inertia ($\mathrm{kg\,m^2}$)
i	electric current (A)
J	current density ($\mathrm{A\,m^{-2}}$)
j	predicted time ahead
k	discrete time
M	molar mass ($\mathrm{kg\,mol^{-1}}$)
N	prediction horizon
P, Q, R	cost function matrices
p	pressure (Pa)
r	reference
T	temperature (K)
t	continues time
U	potential (V)
u	input
V	volume ($\mathrm{m^3}$)
x	state
y	output

Others

$\nabla_\mathrm{t} T$	local temporal temperature gradient ($\mathrm{K\,s^{-1}}$)
$\nabla_\mathrm{x} T$	local spatial temperature gradient ($\mathrm{K\,m^{-1}}$)

Subscripts

$\mathcal{P}$	power
a	air
b	burner
blw	blower
c	heat exchanger cold fluid volume
cell	cell
CH4	methane
CO	carbon monoxide
cp	compressor
cs	control strategy
ct	continuous-time
dt	discrete-time
env	environment
EPC	Electric Power Converter
f	fuel
FAR	Fuel-to-Air Ratio
h	heat exchanger hot fluid volume
H2	hydrogen
HEX	Heat Exchanger
i	current
in	inlet
is	isentropic
LHV	Lower Heating Value
loss	ohmic converter losses
m	motor
max	maximum
min	minimum
nl	nonlinear
O2	oxygen
out	outlet
PEN	Positive-electrode Electrolyte Negative-electrode
rt	real-time
s	sample-time
sim	simulation
SOFC	Solid Oxide Fuel Cell
v	velocity form
w	heat exchanger solid volume

accommodate the dynamic power demands of a vessel, supplementary systems must be appropriately sized, increasing system complexity and restricting the applicability of SOFCs [18,19].

SOFC technology has not yet reached full maturity, and SOFCs are susceptible to damage during dynamic power modulation, particularly with internal reforming. Ensuring safety during transient operation of an SOFC is crucial for the lifetime of the SOFC, but also complex, requiring careful management of gas flows, temperatures and power [20]. The SOFC has to stay within numerous safety limits, such as the fuel utilisation, air utilisation, fuel-to-air equivalence ratio, maximum internal temperatures, and local spatial and temporal temperature gradients [19,21]. The effects of exceeding these limits range from accelerated degradation to a sudden loss of power and adversely affect the overall lifetime and performance of the system [22]. Managing excessive local spatial and temporal temperature gradients in the SOFC

is particularly challenging, as they cannot be measured and require detailed first-principles models to capture their behaviour accurately. Furthermore, their effects on degradation and material failure are not easy to capture and often require experimental testing [23]. Therefore, present control strategies implicitly address the local spatial and temporal temperature gradients by gradually transitioning between different power levels using a rate-of-change limit on the electrical current. This prevents excessive degradation and sudden failure of the system, but the transient behaviour of the SOFC system may require over an hour to stabilise [16]. This makes it impractical for vessels to rely solely on SOFCs for power generation, and a hybrid system will be required to meet all the power requirements of a vessel [18]. Nevertheless, if the power modulation rate of the SOFC can be improved, the SOFC could contribute a larger share to the hybrid system. This would reduce both the overall system complexity and the complexity of its management.

Existing control strategies for SOFC systems predominantly rely on PID control due to its simplicity, robustness, and the widespread understanding of the methodology within the industry [24]. However, the PID controller inherently does not account for safety constraints and is prone to violating them. To mitigate this, the PID methodology can be extended with (dynamic) input saturation and anti-windup techniques to prevent integrator windup [25]. For an SOFC, this can ensure adherence to constraints such as fuel utilisation, air utilisation, and fuel-to-air equivalence ratio [26]. The maximum internal temperature can be maintained within a specific range by carefully tuning the PID controller. However, the PID controller cannot explicitly constrain internal temperatures or account for local spatial and temporal temperature gradients. Therefore, a rate-of-change limit on the electrical current is required when using a PID controller to implicitly constrain the local spatial and temporal temperature gradients in the SOFC. This approach leads to a poor transient response [16].

Model Predictive Control (MPC) has been widely applied in various control problems due to its capability to handle complex nonlinear dynamics, *Multiple-Input Multiple-Output* (MIMO) systems, and tight system constraints [27]. For these reasons, MPC is considered a suitable control strategy for SOFC systems [24]. Furthermore, the implementation of MPC aligns effectively with the optimisation-based energy management strategies currently developed, e.g., [19]. Despite these beneficial capabilities of MPC, previous studies often overlook thermal stress as a critical constraint in SOFC systems. Consequently, existing MPC implementations typically impose simple rate-of-change limits on electrical current rather than fully exploiting MPC's ability to constrain the thermal dynamics.

Contribution

To address this gap, this research proposes the incorporation of a temperature rate-of-change constraint within the MPC strategy. This approach is expected to manage thermal stress during dynamic load tracking more effectively than using conventional current rate-of-change constraints. In particular, this research proposes to:

- Integrate constraints on temperatures and temperature rate-of-change of the SOFC system in the MPC strategy to constrain local spatial and temporal temperature gradients in the SOFC.
- Relax or eliminate the rate-of-change limit on electrical current to enable more flexible power modulation and less conservative transient operation.

Outline

The structure of the paper is as follows: Section 2 reviews the existing literature on control strategies for SOFC systems. Section 3 presents the benchmark SOFC system, including the system modelling, the baseline PID control strategy, and the associated performance metrics. Then, the TC-MPC strategy is formulated in Section 4. Section 5 describes the implementation of the simulation models and the TC-MPC strategy. Section 6 provides the simulation results, comparing the performance of the TC-MPC strategy with that of the baseline PID controller. Finally, Section 7 concludes the paper and offers recommendations for future research.

2. Related work

In early research, the SOFC was primarily introduced for steady-state applications, such as grid-connected systems, where the initial control strategies were developed to maintain a steady-state operating point. Braun [28] describes the objective of controlling the SOFC system as delivering a specific net power while maximising the cell efficiency and ensuring that the SOFC operates within its limits. To do so, Braun identifies three strategies to maintain a steady-state power with the above-described conditions. The first strategy actuates the fuel and air flows to maintain a constant fuel utilisation for either a desired nominal/local stack temperature or an air temperature change. In the second one, the fuel and air flow are varied to regulate a constant cell voltage and desired nominal/local SOFC temperature or an air temperature change. The third strategy delivers fuel and air at a constant rate, and the fuel utilisation and stack temperature will vary according to the required load, where some small variations in the load are assumed. The SOFC stack current is manipulated to regulate output power in all three strategies. Several subsequent publications follow one of these three strategies to control the SOFC system in steady-state as well as for transient control [24].

During transient control, it is crucial to actively manage the SOFC system to stay within the safety limits (e.g. maximum temperature, fuel utilisation and fuel-to-air equivalence ratio). Furthermore, the dynamics of an SOFC system are nonlinear, MIMO, and vastly different in time scale. As a result, the control problem is often divided into energy management, focusing on power delivery and efficiency, and thermal management, concentrating on temperature control and thermal safety. Power control is, for instance, addressed in [29,30] with PID control, but without taking safety limits into account. Li et al. [31] propose an MPC strategy to control the SOFC stack voltage while constraining the fuel utilisation and the fuel flow. Carre et al. [32] developed a feed-forward control strategy incorporating limits on fuel utilisation, air utilisation and air stoichiometry. Temperature control of SOFCs is addressed by Pohjoranta et al. [33], both for a PID controller and an MPC, concluding that the MPC has the potential to reduce thermal stress, but in temperature tracking, it marginally outperforms the PID. Variations in the nominal stack temperature profile are minimised with an $\mathcal{H}_\infty$-controller in [34], concluding that it is impossible to maintain the internal stack temperature profile exactly. Still, the control reduces the variations compared to an open-loop feed-forward strategy. Reineh et al. [35] extend this strategy by including actuator saturation in the synthesis process of the $\mathcal{H}_\infty$-controller. Hajimolana et al. [36] employ a neural network predictive controller to control the temperature of the SOFC stack.

As identified by Pohjoranta et al. [33], power and temperature control use the same inputs and are inherently coupled and changing the power will lead to changes in the temperature. Addressing them separately simplifies the design but leads to conservative transient performance [37]. Therefore, power and temperature controllers are designed sequentially in [20,38] while analysing the coupling between the multiple loops to ensure stability and performance. Stiller [38] develops a multi-mode control strategy based on PID control, controlling both power and temperature. The controller switches between different operation modes to ensure fuel utilisation and voltage constraints. Mueller et al. [20] present a cascaded PID control solution to account for the coupling in power and temperature regulation. These control solutions adequately regulate both power and temperature; however, PID control does not naturally deal with multi-objective control problems,

nor stays within the tight operation range of the SOFC. Therefore, approaches are developed in [39–41] based on MPC strategies to regulate both power and temperature while actively constraining the operation range of the SOFC system. Spivey and Edgar [39] develop an MPC based on an identified second-order linear time-invariant model, which is included in the velocity form to eliminate steady-state offsets. The constraints included the fuel utilisation, air utilisation, temperature, steam-to-carbon ratio and the inputs. The results analyse the radial temperature gradient in a tubular SOFC cell. Sanandaji et al. [40] use a linear parameter-varying model, which is scheduled in the MPC controller based on the current state. Constraints in the MPC include cell voltage, fuel utilisation, and actuator limits. Zhang et al. [41] design an NMPC, where the SOFC model includes a fit of the spatially distributed variables. The minimum current density is constrained. A drawback is that most of these strategies do not include thermal-stress considerations nor analyse the resulting thermal stress due to dynamic power modulation.

Particular works include constraints on the local spatial temperature gradient [39] or include a steady-state optimisation such that the temperature distribution in the SOFC is maintained as close as possible to its nominal condition across all operating power levels [42]. This limits the thermal stress at the steady-state operation point but does not take care of thermal stress during dynamic operation. The related work is summarised in Table 1, showing the control objectives and the included constraints per paper. The table indicates that thermal stress considerations are rarely incorporated in the control strategy and are even less often integrated with power management to balance power tracking and thermal stress.

Incorporating thermal stress into the control strategy is challenging, as it requires complex spatially distributed models to accurately capture both the local spatial and temporal temperature gradients within the SOFC. Previous studies have commonly relied on lumped-parameter models for control design and evaluation, which limits their ability to assess internal thermal effects. This work will investigate to what extent a lumped-parameter model can be utilised to mitigate the local thermal temperature gradient during dynamic operation. Accordingly, a *Thermal-Constrained* (TC)-MPC strategy is proposed, incorporating a constraint on the rate of temperature change. The effectiveness of the TC-MPC is evaluated through simulations on a benchmark SOFC system, using a 1D spatially distributed model to analyse the resulting spatial and temporal temperature gradients due to the dynamic operation. The performance of the TC-MPC will be evaluated against a baseline PID control strategy with an electrical current rate-of-change limit. The research aims to demonstrate that the TC-MPC strategy can modulate the electrical power of the SOFC system significantly faster than the baseline PID strategy while maintaining similar or lower temporal and spatial temperature gradients.

3. Evaluation framework: benchmark system, baseline control, and performance metrics

The benchmark system comprises a generic stand-alone SOFC system with a baseline PID control strategy proposed in [26]. First, the system is introduced, including its configuration, modelling, and operation constraints. Then, the baseline PID control strategy and the performance metrics are discussed.

3.1. Generic stand-alone SOFC system

For maritime applications, the benchmark will focus on a stand-alone SOFC system, meaning that the system is self-sustaining the SOFC operations. The fuel of the SOFC is methane (oxygen-to-carbon ratio of 2.4 and 5% reformed at an, resulting in an inlet composition of CH4 27.1%, CO2 1.42% CO $4.29{\cdot}10^{-3}$%, H2O 65.7% and H2 5.71%). This minimal reforming composition is chosen to emphasise the cooling effect of the internal reforming on the inlet of the SOFC, as a worst-case scenario. During use, the SOFC requires a continuous supply of fuel and air, which must be pre-heated to the SOFC's operating temperature. To facilitate this, the SOFC is equipped with the *Balance of Plant* (BOP), forming an SOFC system. A generic case of such a system is illustrated in Fig. 1. In this configuration, a fuel compressor and air blower manage gas inflows, heat exchangers preheat these inflows, a combustor increases the heat energy in the exhaust gases, and an electrical converter regulates the output power. The SOFC system has three inputs: the compressor torque, blower torque, and requested current, as well as three outputs: fuel utilisation, SOFC temperature, and output power. The following assumptions are relevant for the modelling process:

1. flows are laminar, consisting of ideal and incompressible gases.
2. No side reactions are considered.
3. Each control volume is defined by uniform properties: lumped temperature, pressure, species mole fractions, and molar flow rate.
4. Electrochemistry is considered quasi-static.
5. In a planar co-flow cell, the direction along the flow represents the most critical spatial distribution, regarding the thermal stress.
6. Each cell in the stack is assumed to operate identically with a periodic boundary condition [43], such that a single planar cell simulation is taken as representative of the worst-case scenario inside a full stack with only heat dissipation through the sides of the interconnects.

3.1.1. Air blower and fuel compressor

The air blower and fuel compressor are modelled following the same approach presented in [20,44], where a first-order approximation is used to represent the blower and compressor. It is assumed that a lower-level mass-flow controller shapes this first-order response. The inertia represents the response time, including gas transport. The approach is illustrated for the fuel compressor (abbreviated as cp), but holds similarly for the air blower (abbreviated as blw). The dynamic behaviour is lumped into a single rotating mass, where the rotational velocity ($\omega_{\mathrm{cp}}(t)$) is described as

$$\dot{\omega}_{\mathrm{cp}}(t) = 1/I_{\mathrm{cp}}\left(-C_{\mathrm{cp}}\omega_{\mathrm{cp}}(t) + \tau_{\mathrm{cp}}(t)\right), \tag{1}$$

where I_{cp} is the inertia, C_{cp} is the viscous friction and $\tau_{\mathrm{cp}}(t)$ is the torque. The rotational velocity is linearly related to the resulting molar flow ($\dot{n}_{\mathrm{cp}}(t)$) as

$$\dot{n}_{\mathrm{cp}}(t) = a_{\mathrm{cp}}\omega_{\mathrm{cp}}(t), \tag{2}$$

with a_{cp} the molar flow coefficient. The power consumed by the compressor ($\mathcal{P}_{\mathrm{cp}}(t)$) is modelled via ideal compression work, corrected with a constant thermodynamic efficiency ($\eta_{\mathrm{cp,is}}$) and a constant motor efficiency ($\eta_{\mathrm{cp,m}}$) [45, Chapter 2], as

$$\mathcal{P}_{\mathrm{cp}}(t) = \frac{\dot{n}_{\mathrm{cp}}(t)M_{\mathrm{cp}}c_{\mathrm{p,cp}}T_{\mathrm{cp,in}}}{\eta_{\mathrm{cp,m}}\eta_{\mathrm{cp,is}}}\left[\left(\frac{p_{\mathrm{cp,in}}}{p_{\mathrm{cp,out}}}^{(\gamma-1)/\gamma}\right) - 1\right], \tag{3}$$

where M_{cp} is the molar mass of the molar flow passing the compressor, $c_{\mathrm{c,cp}}$ is the heat capacity of the molar flow, $T_{\mathrm{cp,in}}$ is the inlet temperature of the compressor, $p_{\mathrm{cp,in}}$ and $p_{\mathrm{cp,out}}$ are the inlet and outlet pressures, respectively, and γ is the specific heat ratio.

This model neglects some basic compressor effects, and a more elaborate model that incorporates the neglected effects can be found in [46]. It is assumed that this simplified model captures the overall behaviour of the blower and compressor within the desired operation range of the SOFC system.

3.1.2. Heat exchanger

The heat exchanger dynamics are approximated using a three-control-volume model, representing a layer with hot gases, a layer with cold gases, and a metal separation layer following the approach of [20]. The gases passing through the heat exchanger are subject to enthalpy

Table 1
Overview of the related literature on SOFC control, with TW as This Work.

Contribution	Symbol	Literature														
		[29,30]	[31]	[32]	[33]	[34]	[35]	[36]	[38]	[20]	[39]	[40]	[41]	[26]	[42]	TW
Control objectives																
Power control	$\mathcal{P}_{\text{EPC}}(t)$	x	x	x					x	x	x	x	x	x	x	x
Temperature control	$T_{\text{SOFC}}(t)$				x	x	x	x	x	x	x	x	x	x	x	x
Safety constraints																
Fuel utilisation	$\mu_{\text{f}}(t)$		x	x					x		x	x	x	x		x
Air utilisation	$\mu_{\text{a}}(t)$			x							x		x	x		x
Fuel-to-air equivalence ratio	$\phi_{\text{FAR}}(t)$			x										x		x
SOFC temperature	$T_{\text{SOFC}}(t)$							x			x		x			x
Cell voltage	$U_{\text{cell}}(t)$								x		x	x				x
Input limits	$u(t)$		x	x	x		x	x	x	x	x	x	x	x	x	x
Thermal stress considerations																
Current rate-of-change	$\Delta i_{\text{EPC}}(t)$													x		
Variations w.r.t nominal temperature distribution	$\Delta T_{\text{PEN}}(t)$					x	x								x	
Temperature rate-of-change	$\Delta T_{\text{SOFC}}(t)$															x
Local temporal temperature gradient	$\nabla_{\text{x}} T_{\text{PEN}}(t)$															
Local spatial temperature gradient	$\nabla_{\text{t}} T_{\text{PEN}}(t)$										x					

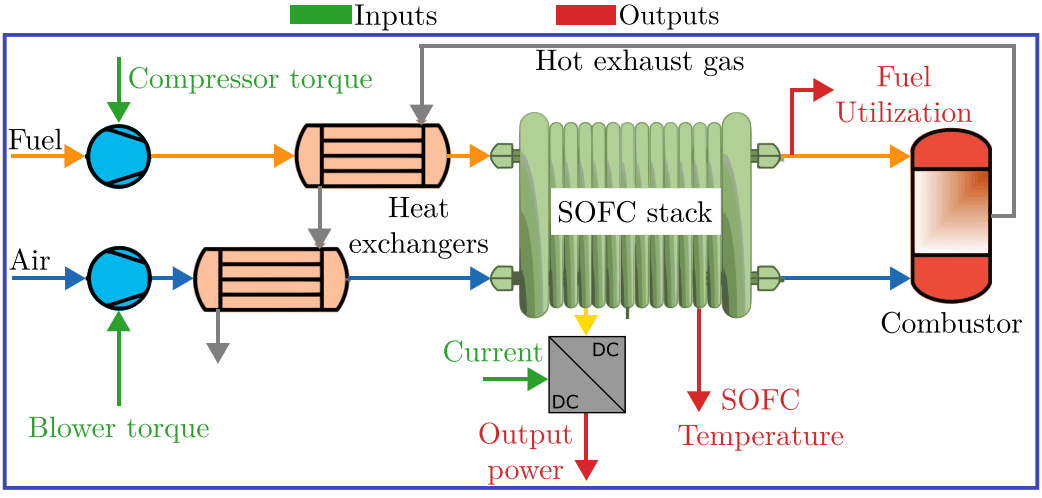

Fig. 1. Generic stand-alone SOFC system overview.

change from the inlet to the outlet and convective heat transfer from the gas layers to the wall. The heat transfer is based on the average of the inlet and outlet temperatures. The heat transfer coefficients are determined based on convective heat transfer between the gases and solids, assuming fully developed laminar flow and accounting for temperature and gas mixture dependencies [43]. This results in the heat exchanger dynamics as

$$\dot{T}_{\text{h}}(t) = \frac{\bar{R}T_{\text{h}}(t)}{p_{\text{h}}V_{\text{h}}\chi_{\text{h}}^{\top}(t)c_{\text{p,h}}(t)}\left[H_{\text{h,in}}(t) - H_{\text{h,out}}(t) + \dot{Q}_{\text{h}}(t)\right], \tag{4a}$$

$$\dot{T}_{\text{w}}(t) = \frac{1}{\rho_{\text{w}}c_{\text{p,w}}V_{\text{w}}}\left[-\dot{Q}_{\text{h}}(t) - \dot{Q}_{\text{c}}(t) - \dot{Q}_{\text{w}}(t)\right], \tag{4b}$$

$$\dot{T}_{\text{c}}(t) = \frac{\bar{R}T_{\text{c}}(t)}{p_{\text{c}}V_{\text{c}}\chi_{\text{c}}^{\top}(t)c_{\text{p,c}}(t)}\left[H_{\text{c,in}}(t) - H_{\text{c,out}}(t) + \dot{Q}_{\text{c}}(t)\right], \tag{4c}$$

$$\dot{Q}_{\text{h}}(t) = \lambda_{\text{h}}(t)A_{\text{h}}\left[T_{\text{w}}(t) - (1/2)T_{\text{h}}(t) - (1/2)T_{\text{h,in}}(t)\right], \tag{4d}$$

$$\dot{Q}_{\text{c}}(t) = \lambda_{\text{a}}(t)A_{\text{c}}\left[T_{\text{w}}(t) - (1/2)T_{\text{c}}(t) - (1/2)T_{\text{c,in}}(t)\right], \tag{4e}$$

$$\dot{Q}_{\text{w}}(t) = \lambda_{\text{w}}A_{\text{w}}[T_{\text{w}}(t) - T_{\text{env}}(t)], \tag{4f}$$

$$H_{\text{h}}(t) = \dot{n}_{\text{h}}^{\top}(t)\bar{H}(T_{\text{h}}(t)), \tag{4g}$$

$$H_{\text{c}}(t) = \dot{n}_{\text{c}}^{\top}(t)\bar{H}(T_{\text{c}}(t)), \tag{4h}$$

where $T_{\text{h}}(t)$, $T_{\text{w}}(t)$, and $T_{\text{c}}(t)$ are the temperatures of the hot gas layer, the solid wall, and the cold gas layer, denoted with the subscripts h, w, and c, respectively. The inlet temperature of the cold gas layer is $T_{\text{c,in}}(t)$, and the inlet temperature of the hot gas layer is $T_{\text{h,in}}(t)$. For each layer, V represents the volume, c_{p} is the heat capacity, H is the enthalpy of the gas mixture and $\dot{Q}$ is the heat flux. The term $\lambda(t)$ is the convective heat transfer coefficient between the solid parts and the gases, which depends on the temperature and the gas concentration, as defined in [43]. The convective heat transfer area is denoted by A. In the hot and cold gas layers, p represents the pressure, $\chi(t)$ is the gas concentration of either the fuel or air flow, $\bar{H}$ is the specific enthalpy of the gas mixture, and $\dot{n}$ is the molar gas flow. These variables are vectors, depending on the number of gases included in the mixture. $\bar{R}$ is the universal gas constant and ρ is the density of the solid wall. The parameters are determined based on the thermal inertia and required SOFC inlet temperatures.

3.1.3. Combustor

The combustor is modelled as a single control volume, where the remaining fuel in the SOFC exhaust is combusted. An adiabatic oxidation is assumed [20,47]. The temperature in the combustor varies

dynamically based on the enthalpy change due to the oxidation as

$$\dot{T}_{\mathrm{b}}(t) = \frac{\bar{R}T_{\mathrm{b}}(t)}{p_{\mathrm{b}}V_{\mathrm{b}}\chi_{\mathrm{b}}^{\top}(t)c_{\mathrm{p,b}}(t)}\left[H_{\mathrm{b,in}}(t) - H_{\mathrm{b,out}}(t) + \dot{Q}_{\mathrm{b}}(t)\right], \tag{5a}$$

$$\dot{Q}_{\mathrm{b}}(t) = \lambda_{\mathrm{b}}(t)A_{\mathrm{b}}[T_{\mathrm{b}}(t) - T_{\mathrm{env}}(t)], \tag{5b}$$

$$H_{\mathrm{b}}(t) = \dot{n}_{\mathrm{b}}^{\top}(t)\bar{H}(T_{\mathrm{b}}(t)), \tag{5c}$$

where $T_{\mathrm{b}}(t)$ is the combustor temperature, $T_{\mathrm{b,in}}(t)$ is the gas inlet temperature, p_{b} is the pressure, V_{b} is the combustor's volume, $\chi_{\mathrm{b}}(t)$ is the gas concentration, $c_{\mathrm{c,p}}(t)$ is the heat capacity and $\dot{n}_b(t)$ is the molar flow through the combustor.

3.1.4. DC–DC converter

The dynamics of the DC-DC converter are significantly faster than the rest of the system (order of μs). Therefore, only the average dynamics are modelled [28,47]. This approach simplifies the current dynamics from a millisecond timescale to several seconds using a low-pass filter with a time constant $t_{\mathrm{EPC}} = 1$ s. Then:

$$\dot{i}_{\mathrm{EPC}}(t) = \frac{-i_{\mathrm{EPC}}(t) + u_{\mathrm{i}}(t)}{t_{\mathrm{EPC}}}, \tag{6}$$

where $i_{\mathrm{EPC}}(t)$ is the electrical current of the converter and u_{i} is the requested electrical current. Furthermore, the ohmic losses of the DC-DC converter are taken into account as

$$\mathcal{P}_{\mathrm{EPC}}(t) = \mathcal{R}_{\mathrm{EPC}}i_{\mathrm{EPC}}(t)^2 \tag{7}$$

with the ohmic resistance $\mathcal{R}_{\mathrm{EPC}}$.

3.1.5. SOFC

A single SOFC cell consists of multiple layers. The electricity generation capabilities come from the *Positive-electrode Electrolyte Negative-electrode* (PEN) structure, where fuel is supplied to the positive electrode via the fuel channel and air to the negative electrode via the air channel, generating a potential between both electrodes. Multiple cells are stacked and electrically connected via a metal interconnect, creating an SOFC stack, denoted in this work in short as the SOFC. In this work, a 1D spatially discretised cell model is used to capture the SOFC stack dynamics as presented in [43]. This model represents a co-flow (electrolyte supported) configuration cell after the Staxera/Sunfire ISM V3.3 short stack. The model discretises the spatial dimension along the direction of flow into successive control volumes with a uniform current density and mass concentrations and temperatures, as shown in Fig. 2. As a result, all variables are spatially distributed, giving insight into the local behaviour of the SOFC, including the spatial and temporal temperature gradient. Each control volume consists of an air channel layer, a PEN structure layer, a fuel channel layer and an interconnect layer. An energy balance governs the temperature in each control volume and layer as

$$\frac{dT_{\mathrm{PEN}}(t,x)}{dt} = \frac{1}{C_{\mathrm{p,PEN}}(t,x)}\left\{\sum_i \lambda_i\left(T_i(t,x) - T_{\mathrm{PEN}}(t,x)\right) + \lambda_{\mathrm{PEN}}\frac{d^2T_{\mathrm{PEN}}(t,x)}{dx^2}\right.$$
$$\left. + \Delta\bar{H}(T_{\mathrm{PEN}}(t,x))r(t,x) - J_{\mathrm{PEN}}(t,x)U_{\mathrm{PEN}}(t) - \dot{Q}_{\mathrm{loss}}(t,x)\right\} \tag{8}$$

with $C_{\mathrm{p,PEN}}$ as the thermal inertial of the PEN structure, $i \in${f,a}, indexes the temperature of the fuel and air in the gas channels, r is the reaction rate of the chemical reactions, J_{PEN} is the current density at the PEN structure interface and U_{PEN} is cell voltage. The SOFC temperature in the 1D model is the stacked vector of the temperature in each layer for all control volumes as $T_{\mathrm{SOFC}}(t) = [T_{\mathrm{a}}^{\top}(t),\ T_{\mathrm{PEN}}^{\top}(t),\ T_{\mathrm{f}}^{\top}(t),\ T_{\mathrm{IC}}^{\top}(t)]^{\top}$. A mass balance is solved dynamically in the air channel and fuel channel layers of each control volume based on the mass concentration in the fuel and air channel layers as $\chi_{\mathrm{SOFC}}(t) = [\chi_{\mathrm{f}}^{\top}(t),\ \chi_{\mathrm{a}}^{\top}(t)]^{\top}$. The electrochemistry resolves the cell voltage and current density distribution ($J_{\mathrm{PEN}}(t)$) based on the temperature and concentration distribution along the SOFC stack. This is either solved statically as a system of algebraic equations [43,48] or approximated with an ordinary differential equation as in [49, Chapter 6]. To keep this concise, further details are omitted and can be found in [43]. In [43], the 1D spatially discretised SOFC model is validated by means of current power curves from manufacturers' data for various fuel compositions and the spatial distribution of the reaction rates is validated with a 3D CFD model. Both show the validity of the SOFC model.

Table 2
Operational constraints for the SOFC benchmark system.

Constraint name	Symbol	Value	Unit
Fuel utilisation	$\mu_{\mathrm{f}}(t)$	≤ 0.80	[–]
Air utilisation	$\mu_{\mathrm{a}}(t)$	≤ 0.60	[–]
Fuel-to-air equivalence ratio	$\phi_{\mathrm{FAR}}(t)$	≤ 0.50	[-]
PEN temperature	$T_{\mathrm{PEN}}(t)$	geq 923 ≤ 1133	[K]
Cell voltage	$U_{\mathrm{PEN}}(t)$	≥ 0.6	[V]
Current density	$J_{\mathrm{PEN}}(t)$	≤ 3000	[A/m^2]

3.1.6. System description

All the components are connected following the system configuration in Fig. 1. The outputs of the system are the fuel utilisation, SOFC temperature and output power. The fuel utilisation ($\mu_{\mathrm{f}}(t)$) is determined as

$$\mu_{\mathrm{f}}(t) = \frac{I_{\mathrm{EPC}}(t)}{2\mathcal{F}(\chi_{\mathrm{H2}} + \chi_{\mathrm{CO}} + 4\chi_{\mathrm{CH4}})\dot{n}_{\mathrm{cp}}(t)}, \tag{9}$$

with $\mathcal{F}$ as the Faraday constant. The output power ($\mathcal{P}_{\mathrm{out}}$) of the SOFC system is determined by the power generated by the SOFC stack minus the auxiliary losses, e.g., the power consumed by the air blower, fuel compressor and the DC-DC converter losses, which can be modelled as

$$\mathcal{P}_{\mathrm{out}}(t) = U_{\mathrm{PEN}}(t)I_{\mathrm{EPC}}(t) - \mathcal{P}_{\mathrm{cp}}(t) - \mathcal{P}_{\mathrm{blw}}(t) - \mathcal{P}_{\mathrm{loss}}(t), \tag{10}$$

and the overall electrical efficiency (η(t)) of the SOFC system is determined as

$$\eta(t) = \frac{\mathcal{P}_{\mathrm{out}}(t)}{\Delta\bar{H}_{\mathrm{LHV}}\dot{n}_{\mathrm{cp(t)}}}. \tag{11}$$

where $\bar{H}_{\mathrm{LHV}}$ is the lower heating value of the fuel at the inlet of the system.

The model of the overall system, the SOFC stack and the BOP can be written in general nonlinear continuous-time state-space form as

$$\Sigma_{\mathrm{nl,ct}} : \begin{cases} \dot{x}(t) = f(x(t), u(t)) \\ y(t) = h(x(t)) \end{cases}, \tag{12}$$

where $x(t) \in \mathbb{R}_{\mathrm{x}}^{\mathrm{n}}$ is the composite state vector, i.e., $x(t) \triangleq [\omega_{\mathrm{cp}}^{\top}(t),\ \omega_{\mathrm{blw}}^{\top}(t),\ T_{\mathrm{HEX,f}}^{\top}(t),\ T_{\mathrm{HEX,a}}^{\top}(t),\ T_{\mathrm{b}}^{\top}(t),\ T_{\mathrm{SOFC}}^{\top}(t),\ \chi_{\mathrm{SOFC}}^{\top}(t),\ J_{\mathrm{PEN}}(t)^{\top}]^{\top}$, with $T_{\mathrm{HEX,f}}$ as the three temperatures for the fuel heat exchanger and $T_{\mathrm{HEX,a}}$ as the three temperatures of the air heat exchanger. Moreover, $u(t) \in \mathbb{R}_{\mathrm{u}}^{\mathrm{n}}$ is the composite input vector, i.e., $u(t) \triangleq [\tau_{\mathrm{cp}}(t),\ \tau_{\mathrm{blw}}(t),\ u_{\mathrm{i}}(t)]^{\top}$, and $y(t) \in \mathbb{R}_{\mathrm{y}}^{\mathrm{n}}$ is the composite output vector of the system, i.e., $y(t) \triangleq [\mu_{\mathrm{f}}(t),\ T_{\mathrm{SOFC}}(t),\ \mathcal{P}_{\mathrm{out}}(t)]^{\top}$. For the SOFC system, there exists a feasible operating region, which is defined by the compact sets $\mathbb{X} \subset \mathbb{R}_{\mathrm{x}}^{\mathrm{n}}$, $\mathbb{U} \subset \mathbb{R}_{\mathrm{u}}^{\mathrm{n}}$ and $\mathbb{Y} \triangleq \{h(x(t)) : x(t) \in \mathbb{X}\}$.

3.2. Operational constraints

The following constraints are considered in the SOFC system: fuel utilisation, air utilisation, fuel-to-air equivalence ratio, maximum and minimum PEN temperature, and minimal cell voltage, as summarised in Table 2. These constraints are based on the Staxera/Sunfire ISM V3.3 and are included to prevent degradation effects in the SOFC due to side reactions (e.g., carbon decomposition or nickel oxidation) or mechanical stress [20,21]. It should be noted that this stack is robust

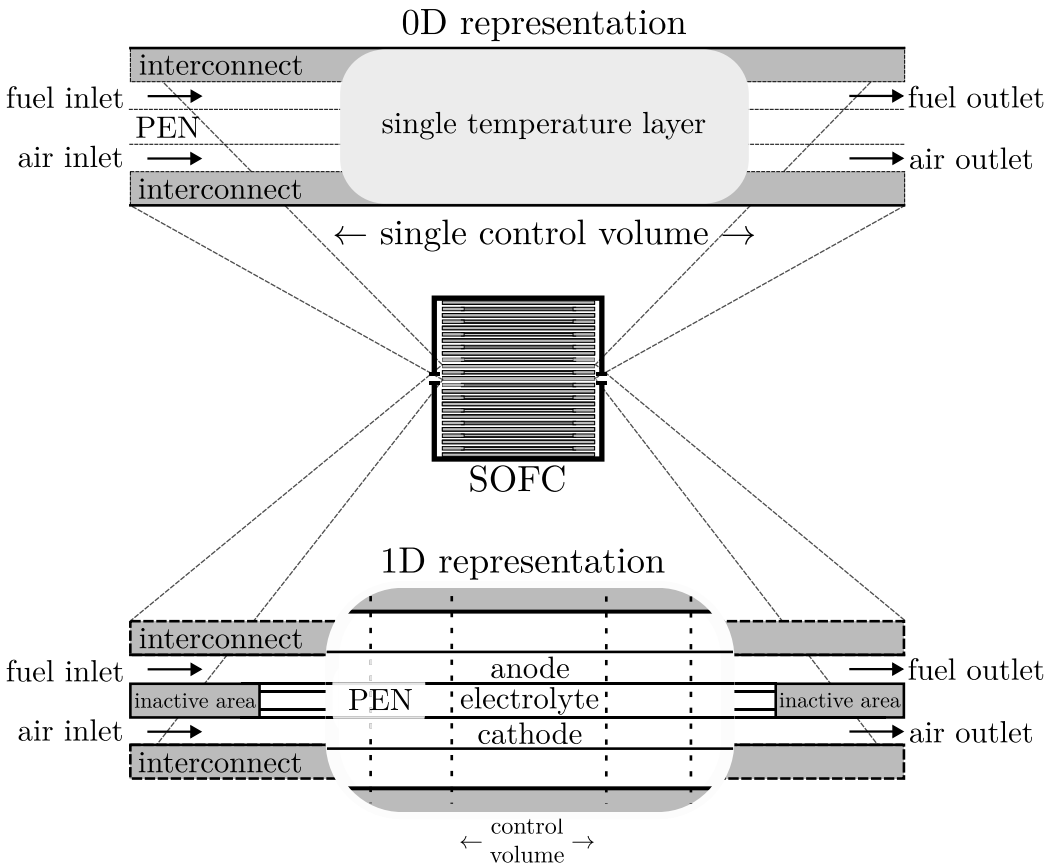

Fig. 2. Schematic overview of the 1D and 0D SOFC model, illustrating the layers and spatial distribution for the 1D model and how these are all lumped in the 0D model.

and tolerates extreme operational conditions. Therefore, these constraints are not applicable to any general SOFC stack. Furthermore, note that the constraints on the PEN temperature mean that the minimum temperature has to stay above 923 [K] and the maximum temperature under 1133 [K], not that the mean/measured temperature will vary between these constraints. The air utilisation ($\mu_a(t)$) and fuel-to-air equivalence ratio ($\phi_{FAR}(t)$) are determined, respectively as

$$\mu_a(t) = \frac{i(t)}{4\mathcal{F}\chi_{O2}\dot{n}_{blw}(t)}, \tag{13}$$

$$\phi_{FAR}(t) = \frac{(\chi_{H2} + \chi_{CO} + 4\chi_{CH4})\dot{n}_{cp}(t)}{2\chi_{O2}\dot{n}_{blw}(t)}. \tag{14}$$

3.3. Baseline PID controller

A PID controller is used as the baseline, given its widespread application in SOFC systems [24] and industry. Furthermore, in [26] it is also shown that a well-designed PID strategy gives a similar performance as an MPC with a *Current Rate-of-change Limit* (CRL). The MPC can only excel over the PID if it can leverage one of its advanced properties. This is not the case if the thermal stress is mitigated by using a CRL. Therefore, PID is a relevant baseline control strategy. Following the approach of [26], a safety-saturated PID controller is designed. This consists of three PID controllers: one for the fuel utilisation, one for the SOFC temperature and one for the output power. For the PID controller, the SOFC temperature is chosen as the air temperature at the outlet of the SOFC. The inputs of the SOFC system are coupled so that controlling power regulates the electrical current and simultaneously adjusts the fuel and air flow based on fixed air and fuel utilisation. The temperature PID supplies additional air based on the temperature set-point and the fuel utilisation adjusts the fuel flow based on the desired fuel utilisation. To ensure the safety of the SOFC system and adherence to the constraints, the output of the PID controller is saturated. This keeps the maximum and minimum inputs, the fuel utilisation and the fuel-to-air equivalence ratio within specified limits. Additionally, to limit the local spatial and temporal temperature gradients in the SOFC, a CRL is implemented by appropriately saturating the controller outputs. Back-calculation is employed to prevent integral windup. The structure of the PID controller is shown in Fig. 3. The PID controller parameters are tuned via a fixed-structure LPV synthesis procedure based on a local LPV representation of the SOFC system model. This tuning method is chosen over tuning by hand and sequential loop-shaping for its robustness and systematic incorporation of the desired performance [50]. More details on the LPV modelling and the synthesis procedure can be found in [26].

3.4. Key performance indicators

In this research, the performance of the control strategies with the benchmark system is assessed with five *key performance indicators* (KPIs). Power tracking is the primary objective of the SOFC system, denoted as

$$\Pi: \quad 1 - \frac{1}{t_{sim}} \int_{t=0}^{t_{sim}} \|\bar{r}_{\mathcal{P}}(t) - \bar{\mathcal{P}}_{out}(t)\|^2 dt. \tag{15}$$

The KPI integrated the tracking error to obtain the average tracking error, which is subsequently subtracted from 1 to obtain the tracking precision on a normalised scale between 0 and 1. Here, 1 means perfect tracking.

To evaluate the thermal stress during transient operation of the SOFC, the maximum spatial and temporal temperature gradient in the

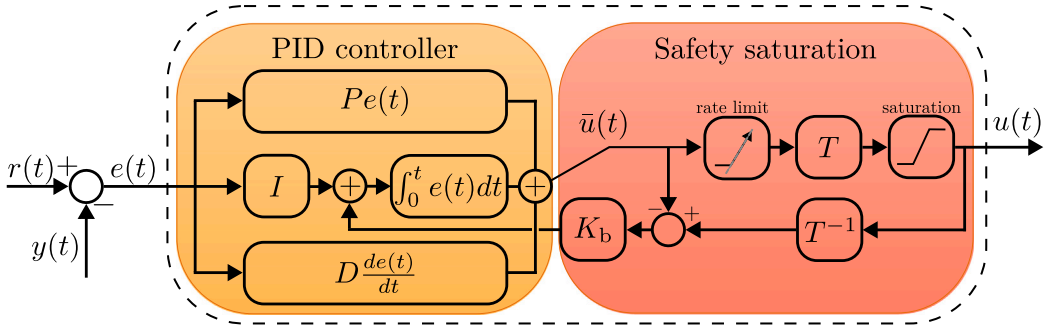

Fig. 3. Overview of the safety-saturated PID controller.

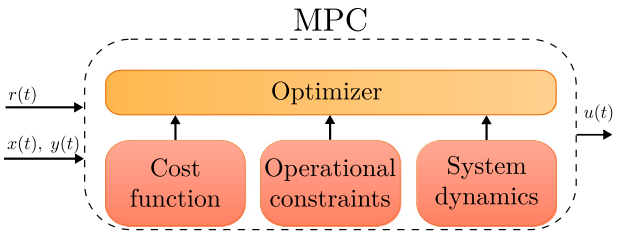

Fig. 4. Overview of the TC-MPC controller.

PEN structure of the SOFC is determined, respectively as

$$\nabla_x \bar{T}: \quad \max\left(\frac{dT_{\mathrm{PEN}}(t,x)}{dx}\right), \tag{16}$$

$$\nabla_t \bar{T}: \quad \max\left|\frac{dT_{\mathrm{PEN}}(t,x)}{dt}\right|. \tag{17}$$

Lower values for these KPIs are desirable as they result in less thermal stress and a longer lifetime.

A longer lifetime should not be traded for a significant electrical efficiency decrease, and therefore the overall efficiency is measured as

$$\bar{\eta}: \quad \frac{1}{t_{\mathrm{sim}}}\int_{t=0}^{t_{\mathrm{sim}}} \eta(t)dt. \tag{18}$$

To demonstrate the practical applicability of the MPC, the real-time CPU ratio is reported as the percentage of the sampling time needed to perform the next input computation:

$$\phi_{\mathrm{rt}}: \quad \frac{1}{t_{\mathrm{sim}}}\int_{t=0}^{t_{\mathrm{sim}}} \frac{t_{\mathrm{cs}}(t)}{t_{\mathrm{s}}}dt. \tag{19}$$

4. Thermal-constrained MPC

An MPC operates fundamentally differently from a PID controller. While a PID adjusts the system based on the current error signal, an MPC predicts future system behaviour using a dynamic model and minimises a cost function over a prediction horizon, as shown in Fig. 4. This predictive approach enables the MPC to anticipate and respond proactively to changes in load requests, provided future reference values are available. Additionally, MPCs can incorporate hard constraints on system behaviour, offering greater control flexibility and safety.

MPC relies on a prediction model. Using the benchmark SOFC system model described in (12) as a prediction model in the MPC results in an intractable optimisation problem due to the model's high complexity. To address this, the 1D spatially discretised SOFC model with 968 states is simplified to a 0D SOFC model containing only a single state. In the 0D model, all layers and distributed variables of the spatially discretised 1D model are lumped into a single layer and one control volume, as illustrated in Fig. 2, in which a dynamic energy balance is solved to obtain the temperature dynamics ($T_{\mathrm{SOFC}}(t)$). The mass balance resolves the molar flow and reaction rates statically, resulting in the mass concentration ($\chi_{\mathrm{SOFC}}(t)$). The electrochemistry determines the cell voltage ($U_{\mathrm{cell}}(t)$) and current density ($J_{\mathrm{SOFC}}(t)$) based on the Nernst equation and includes a temperature-dependent fit for the ohmic losses. A full model description is presented in [51], as well as a comparison between the 0D model and the 1D spatially discretised model. This shows that the 0D model exhibits the same general behaviour as is expected from a lumped-parameter model. Replacing the spatial discretised 1D model for the 0D SOFC model in the SOFC system gives the full MPC prediction model in the same form as (12). This simplification introduces a model mismatch between the benchmark simulation model and the prediction model, where the effectiveness of the MPC relies heavily on the accuracy of the prediction model [52]. In the case of SOFC, the output voltage and power are influenced by internally distributed parameters that the simplified prediction models cannot fully capture [51], due to its 0D representation. As a result, a mismatch between the predicted output with the MPC and the actual SOFC system output is inevitable, and the standard tracking MPC scheme, e.g. [53], will result in an unsatisfactory tracking error. A reliable way to achieve accurate output tracking is to incorporate output feedback through an offset-free MPC algorithm, utilising the discrete-time velocity form of the system [54]. First, the discrete-time dynamics are obtained as

$$\Sigma_{\mathrm{nl,dt}}: \begin{cases} x_{k+1} &= F(x_k, u_k) \\ y_k &= h(x_k) \end{cases}, \tag{20}$$

which is obtained by integrating the continuous-time system (12) using the fourth-order Runge–Kutta method, with $t = kt_{\mathrm{s}}$ and the sample time t_{s}. The discrete-time velocity form of a discrete-time nonlinear system is then given as

$$\Delta\Sigma_{\mathrm{v,dt}}: \begin{cases} \Delta x_{k+1} &= \mathcal{A}(\xi_k)\Delta x_k + \mathcal{B}(\xi_k)\Delta u_k \\ \Delta y_k &= C(\xi_k)\Delta x_k \end{cases}, \tag{21}$$

with the discrete state velocity as $\Delta x_{\mathrm{k}} = x_{\mathrm{k}} - x_{\mathrm{k-1}}$, the discrete input velocity as $\Delta u_{\mathrm{k}} = u_{\mathrm{k}} - u_{\mathrm{k-1}}$, $\xi_k = [x_k^\top,\ x_{k-1}^\top,\ u_k^\top,\ u_{k-1}^\top]^\top$, and $\mathcal{A}(\xi_k), \mathcal{B}(\xi_k), C(\xi_k)$ are as defined in [55]. With the model expressed in this form, an offset-free tracking MPC is formulated as

$$\begin{aligned} \min_{x_{\cdot|k}, y_{\cdot|k}, u_{\cdot|k}} \quad & \|[\Delta x_{N|k}, r_{N|k} - y_{N|k}]\|_P + \\ & \textstyle\sum_{j=0}^{N-1} \|r_{j|k} - y_{j|k}\|_Q + \|\Delta u_{j|k}\|_R, \\ \text{s.t.} \quad & \Delta x_{j+1|k} = \mathcal{A}(\xi_{j|k})\Delta x_{j|k} + \mathcal{B}(\xi_{j|k})\Delta u_{j|k}, \\ & y_{j+1|k} = C(\xi_{j+1|k})\Delta x_{j+1|k} + y_{j|k}, \\ & x_{j+1|k} = \Delta x_{j+1|k} + x_{j|k}, \\ & u_{j|k} = \Delta u_{j|k} + u_{j-1|k}, \\ & x_{j|k} \in \mathbb{X}, \\ & u_{j|k} \in \mathbb{U}, \\ & \Delta x_{j|k} \in \mathbb{X}_\Delta \\ & x_{0|k} = x(t), \\ & y_{0|k} = y(t), \\ & u_{-1|k} = u(t - t_{\mathrm{s}}), \\ & \Delta x_{0|k} = \Delta x(t), \\ & j \in \mathbb{Z}_{[0,N]} \end{aligned} \tag{22}$$

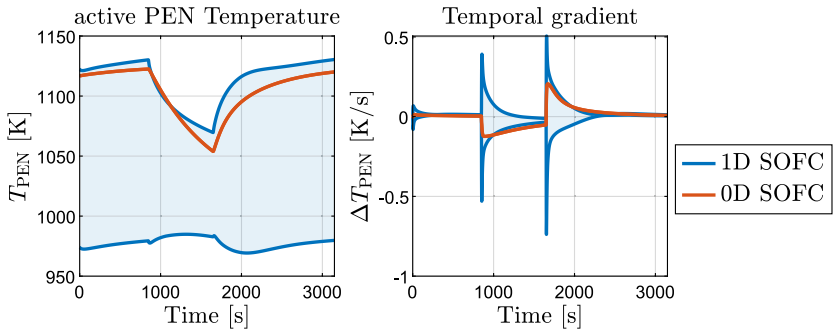

Fig. 5. Comparison of the SOFC temperature behaviour in the 0D predicted model and the 1D simulation model.

with r_k as the desired reference for the output y_k, Q, R, P as positive semi-definite cost matrices, N as the prediction horizon, the subscript j is the predicted time ahead, the subscript $\cdot|k$ denotes the full prediction horizon and $\mathbb{X}_\Delta$ is the set of constraints on the discrete state velocity. The dependencies of $\mathcal{A}, \mathcal{B}, \mathcal{C}$ on ξ_k are nonlinear. In this case, $\mathcal{A}(\xi_k), \mathcal{B}(\xi_k), \mathcal{C}(\xi_k)$ are estimated based on the previous solution as described in Algorithm 1, allowing to solve the MPC in one iteration [56]. This gives the MPC modest computational effort and allows for real-time implementation.

Algorithm 1 Offset-free tracking MPC scheme

Require: $r(t)\ \forall t \in [0, t_{sim}]$

1: Initialize states $x(0)$, inputs $u(-t_s)$, and initial guess input, state and output trajectory $u^*_{\cdot|0}$, $x^*_{\cdot|0}$, $y^*_{\cdot|0}$
2: **for** $t = [0, t_{sim}]$ **do**
3: Measure $x(t)$ and $y(t)$ at $t = kt_s$.
4: Determine $\mathcal{A}(\xi_{\cdot|k})$, $\mathcal{B}(\xi_{\cdot|k})$ and $\mathcal{C}(\xi_{\cdot|k})$, based on previous solution $x^*_{\cdot|k-1}$, $u^*_{\cdot|k-1}$ and $y^*_{\cdot|k-1}$
5: Solve Eq. (22)
6: Apply $u(t+\theta) = u^*_{0|k}$, $\theta \in [0, t_s)$
7: **end for**

In the MPC formulation $\Delta x_{i|k} \in \mathbb{X}_\Delta$ constrains the rate-of-change for the temperatures in the system. In the 0D SOFC prediction model, this is equivalent to constraining the temporal temperature gradient. However, as the 0D prediction model assumes a uniform temperature throughout the SOFC, this does not constrain the local temporal temperature gradient in the simulation benchmark model. To analyse the performance of the 0D SOFC prediction model, the temperature dynamics of the 0D SOFC model and the 1D spatially distributed SOFC model are compared by means of an open-loop ramp-up ramp-down simulation. The resulting temperature and temporal temperature gradient are given in Fig. 5. The 0D SOFC model is designed to predict the outlet temperature, which is slightly lower than the maximum temperature. Furthermore, the figure shows that the 0D model captures the overall behaviour of the temporal temperature gradient but misses the local behaviour, which leads to the instant peaks and the spatial temperature distribution. This is a fundamental limitation of using the 0D prediction model due to its lumped nature. Nevertheless, by applying soft constraints on the temperature rate-of-change in the MPC prediction model, the maximum local temporal temperature gradient observed in the 1D spatially discretised model during simulation can be reduced. Additionally, the results will demonstrate that these rate-of-change constraints on the temperature will limit the power tracking capabilities, where tighter rate-of-change constraints result in less dynamic tracking behaviour. This is similar to the CRL in the baseline PID but allows more flexibility in power tracking.

5. Implementation

The benchmark simulation model is implemented in MATLAB, and the simulations are executed with the ode15s solver. A maximum step-time of 1 [s] is chosen to simulate all dynamics in the benchmark model accurately.

Table 3
CRL variations for the PID controller.

PID	CRL-1	CRL-2	CRL-3	CRL-4
$\|\|\Delta i_{EPC}(t)\|\|$ [A/s]	≤ 1	$\leq \frac{1}{10}$	$\leq \frac{1}{15}$	$\leq \frac{1}{30}$

The baseline PID controller is implemented in MATLAB in the continuous-time as well. It is assumed that any hardware is fast enough to accurately sample the PID controller in discrete-time, as the fastest dynamics are around 1 [s]. For efficient operation, the references for the fuel utilisation and the SOFC temperature should be close to the constraint. Therefore, the fuel utilisation reference is set as 0.75 [-]. The PID controller will operate on output feedback and track the air temperature at the outlet of the SOFC, where a reference air outlet temperature of 1093 [K] ensures that the maximum temperature will not violate the constraint of a maximum SOFC temperature of 1133 [K], but ensures operation close to the constraint. The PID strategy is configured with four values for the CRL, to evaluate the impact of varying power modulation rates on the resulting local spatial and temporal temperature gradients in the SOFC. These CRL values are listed in Table 3. The slowest CRL ($\Delta i_{EPC}(t) \leq \frac{1}{30}$) corresponds to the ramping rate allowed by the manufacturer [57]. The remaining three ramping rates are increased to demonstrate the potential improvements in power tracking and the associated spatial and temporal temperature gradients if faster regulation were allowed.

The TC-MPC is implemented in MATLAB, using the CasADi toolbox [58], and is solved with IPOPT. The fuel utilisation reference is the same as for the baseline PID (0.75 [-]). To be able to constrain the maximum temperature and limit the local temporal temperature gradient in the SOFC, the TC-MPC needs the maximum SOFC temperature, which is not measurable. In [59], a Kalman filter is developed where the maximum temperature is estimated with an error that stays within 2 [K] over a 6-hour prediction horizon. The estimate improves significantly for shorter horizons. In this study, the simulated values are directly provided to the MPC, and it is assumed that an estimation filter, as discussed above, could provide an accurate estimate. The design of a specific filter for this system is left for future work. Instead, the emphasis is placed on the design of the MPC. This gives a maximum SOFC temperature reference of 1123 [K], corresponding with a 30 [K] temperature difference between the maximum SOFC temperature and the air outlet temperature. The values for the Q and R are manually selected by trial and error to obtain similar tracking behaviour as the baseline PID. P is the solution of the *Discrete-time Algebraic Riccati Equation* (DARE). This results in strict output power tracking and relatively more freedom for fuel utilisation and SOFC temperature to diverge from the reference if beneficial. The values for these matrices are given in Table 4. The prediction horizon is chosen as $N = 20$ with a sampling time $t = 1$ [s] as a trade-off between computational

Table 4
Simulation parameters for the TC-MPC.

Parameter	Value
Q	$\text{diag}([4 \cdot 10^3, 1 \cdot 10^2, 5 \cdot 10^4])$
R	$\text{diag}([0.25, 1 \cdot 10^2, 1 \cdot 10^{-3}])$
P	Solution of the DARE
N	20
t_s	1 [s]

Table 5
Constraint variations for the TC-MPC.

MPC	$\Delta T_{\text{SOFC}}(t)$ [K/s]		$\Delta T_{\text{c,f}}(t)$ [K/s]		$\Delta T_{\text{c,a}}(t)$ [K/s]	
	min	max	min	max	min	max
TC-1	−0.37	0.40	−5.00	5.00	−3.00	6.00
TC-2	−0.37	0.37	−1.50	3.00	−0.70	3.00
TC-3	−0.32	0.32	−1.10	2.00	−0.50	2.00
TC-4	−0.22	0.13	−0.60	1.30	−0.22	1.00

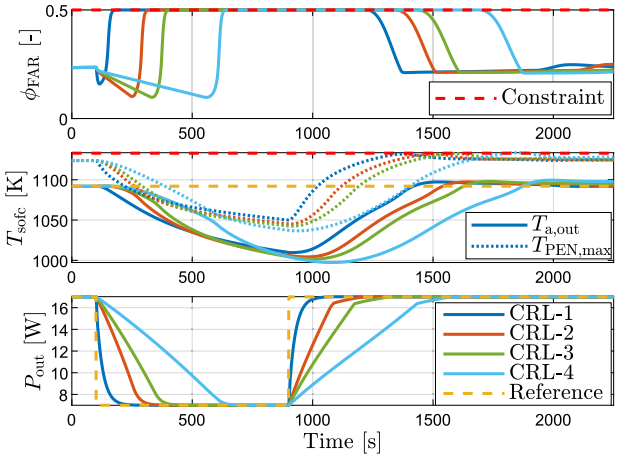

Fig. 6. Temperature and power tracking with the safety-saturated PID controller for different current rate limits.

complexity and prediction accuracy. The TC-MPC is implemented with four sets of temperature rate-of-change constraints to demonstrate the sensitivity of TC-MPC rate-of-change constraints on the local temporal temperature gradients and the dynamic power tracking. Furthermore, values for these constraints are manually selected by trial and error such that the resulting maximum temporal temperature gradients in the benchmark simulation correspond to the results of the baseline PID controller. This results in the four sets as given in Table 5. There exist systematic approaches to obtain the TC-MPC parameters and optimise the behaviour of the TC-MPC for a specific application, e.g., learning-based approaches [60]. Here, the manually selected values suffice for the purpose of this research, as the results will indicate.

All simulations are performed on a Dell Latitude 7430 with an Intel® 12th Gen i7-1265U CPU @1.80 GHz and 16 GB RAM.

6. Results

Both the TC-MPC and the baseline PID strategy are simulated operating the benchmark system model. Two different scenarios are simulated, and the potential performance is investigated using the four sets of rate-of-change constraints. The KPIs resulting from the TC-MPC are compared to the KPIs from the baseline PID. This research evaluates the sensitivity of the rate-of-change constraints with respect to the power tracking capabilities and the maximum local temporal and spatial temperature gradients in the SOFC. The first scenario is a short simulation focused on qualitative analysis for a ramp-down and ramp-up between the maximum and minimum load. In the second scenario, the controllers will track a longer load cycle, such that KPIs can be analysed quantitatively.

6.1. Scenario 1: Ramp-down and ramp-up

The first scenario consists of a ramp-down from the maximum single-cell load (17 [W]) to the minimum single-cell load (7 [W]) in 800 [s], a ramp-up back to the maximum load and the system's power and temperature are stabilised within 1500 [s]. The SOFC temperature is regulated as mentioned above, and the fuel utilisation is controlled at 0.75 [-].

The scenario is simulated with the four baseline PID controllers. The results are given in Fig. 6, showing adequate power tracking for each of the CRLs. Varying modulation rates can be observed during the power ramp-up, with the slope determined by the CRL. When the controller approaches the maximum current, the SOFC system has not yet reached its maximum power output, as the temperature continues to rise towards its set-point, which defines the last slope of the ramp. The air outlet temperature is maintained at the desired 1093 K at maximum load. However, at minimum load, the fuel-to-air equivalence ratio constraint is reached, causing the temperature to drop since the cooling airflow cannot be reduced further.

The resulting temperature dynamics in the PEN structure are shown in Fig. 7. The PEN temperature stays within the maximum and minimum constraints, and one can observe that a slow power modulation results in more cooling and, thus, a lower minimum SOFC temperature. Interesting to note is that the different CRLs do not result in significant variations of the spatial temperature gradient in the PEN structure. The maximum and minimum spatial gradients are the same. This suggests that the spatial temperature gradient is not influenced by the manner of dynamic operation, but varies with the power set-point due to corresponding changes in absolute temperature. As a result, the spatial temperature gradient can be linked to the operational set-point. In case of the PID control strategy, this is managed by the reference set-point. Considerable deviations are observed in the local temporal temperature gradient, revealing a clear relationship: a higher CRL leads to a higher maximum and minimum local temporal temperature gradient. These results clearly show that there is a trade-off between the dynamic power tracking and the maximum local temporal temperature gradient. Where fast power tracking results in high temporal temperature gradients and vice versa. This also means that in this way, faster tracking comes at the cost of higher degradation.

The thermal constraints of the TC-MPC controllers TC-1–TC-4 are specifically chosen, such that the resulting local temporal temperature gradient in the SOFC matches that of the one resulting from the corresponding PID controller CRL-1–CRL-4. The current rate constraint in the TC-MPC is relaxed to allow for faster power modulation with respect to the PID controllers when allowed by the thermal constraints. Fig. 8 compares the TC-MPC controllers with the baseline PID and corresponding CRL for the ramp-up ramp-down scenario. The figure illustrates that the TC-MPC improves load tracking while the maximum local temporal temperature gradient either remains unchanged or decreases. The KPIs for the ramp-up ramp-down scenario are shown in Fig. 9, verifying the results from Fig. 8. The TC-MPC improves the load tracking between 7%–17% for TC-2–TC-4 when compared to the baseline PID strategy with CRL-2–CRL-4, without a significant difference in local temporal and spatial temperature gradient in the SOFC. TC-1 improves the tracking performance marginally with 1%, but decreases the local temporal temperature gradient with 0.14 [K/s], due to the specific values for the thermal constraints. The percentages are improvements of the TC-MPC power tracking with respect to the power tracking of the CRL-PID. As concluded earlier, both the PID and TC-MPC control strategies do not affect the spatial temperature gradient. This is verified with the spatial gradient KPI, which does not significantly change over the various rate-of-change constraints. Overall, the KPIs show a marginal increase in the spatial temperature

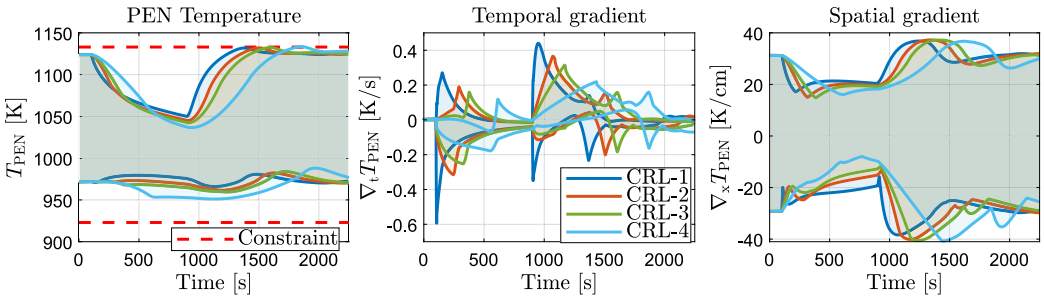

Fig. 7. PEN temperature (gradients) for the safety-saturated PID controller with various current rate limits.

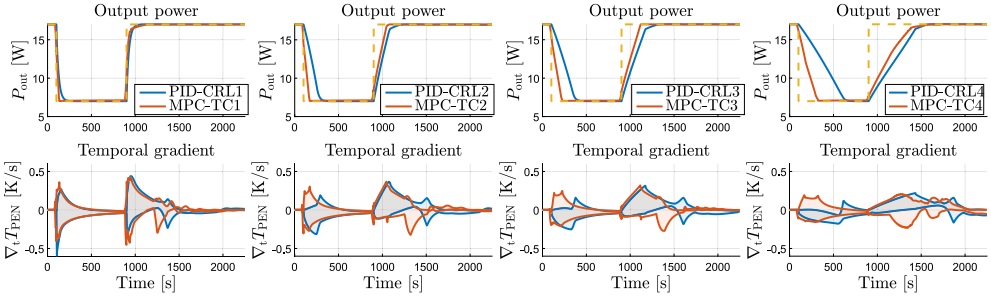

Fig. 8. Comparison of load tracking and temporal temperature gradient for the TC-MPC and CRL-PID.

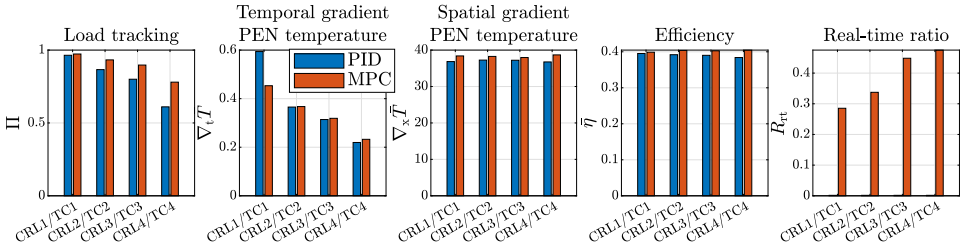

Fig. 9. Performance indicators for simulation scenario 1.

gradient and efficiency for the TC-MPC. The TC-MPC maintains the initial high temperature better than the PID, resulting in an overall higher temperature, slightly increasing the spatial temperature gradient and efficiency. However, the TC-MPC does not optimise for more efficient operation and does not improve the efficiency in general. As expected, the TC-MPC increases the real-time CPU ratio from an average of $4.8 \cdot 10^{-5}$ for the baseline PID to 0.39, which is significant but real-time feasible. The values for the KPIs are included in Table A.1 in the appendices.

The idea behind the improvement is that a power change with the PID strategy results in an immediate peak in the local temporal temperature gradient and a much slower temperature change after this peak. In contrast, the TC-MPC tries to regulate the power, such that the SOFC temperature changes at a constant maximum rate-of-change over the full transient. This is partly what can be observed in Fig. 8. However, the prediction model of the TC-MPC is 0D and is not able to accurately predict the local temperature behaviour of the SOFC, only the overall temperature behaviour of the SOFC. Therefore, the observed maximum local temporal temperature gradient is not constant during the power transient. This indicates that the TC-MPC strategy and the SOFC power tracking could be even further improved with a more accurate prediction model.

6.2. Scenario 2: Load cycle

The second scenario comprises a sequence of 20 random load set-points, changing every 200 [s] to mimic the power request from an energy management strategy. Both the baseline PID and the TC-MPC strategy are simulated for the load cycle. The power tracking and local temporal temperature gradients are shown in Fig. 10, and the corresponding performance indicators in Fig. 11. The results of the load cycle are not one-to-one comparable with the results from the first scenario. Still, the KPIs indicate that the TC-MPC improves load tracking with respect to the baseline PID with 5%–17%, while reducing the maximum local temporal temperature gradient between 0.067 and 0.097 [K/s]. In particular, controller TC-4 improves the load tracking performance considerably over CRL-4, where CRL-4 is not able to complete some of the load steps. Similarly to scenario 1, the maximum local spatial temperature gradient and efficiency do not vary significantly. The real-time CPU ratio is 0.44 [-] or less, similar to scenario 1. The calculated KPIs are given in Table A.2 in the appendices. The results indicate that the TC-MPC improves the load-tracking capabilities of the SOFC system over the CRL-PID without increasing the thermal stress in the SOFC. Furthermore, the results indicate that the spatial temperature gradient is unaffected by the manner of dynamic operation. This suggests that the temporal temperature gradient is the critical limiting indicator of thermal stress during dynamic load tracking. The spatial gradient can be related to the absolute power and temperature set-point. The results also clearly indicate room for further improvement. The 0D model is far from perfect in predicting the maximum temporal temperature gradient of the 1D SOFC model. As a result, the temporal temperature gradient of the 1D SOFC model is effectively reduced but not constrained. A more accurate prediction of the temporal temperature gradient would allow

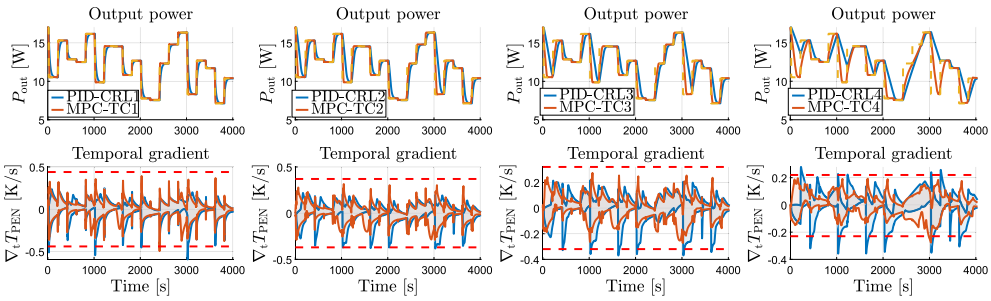

Fig. 10. Comparison of load tracking and temporal temperature gradient for scenario 2.

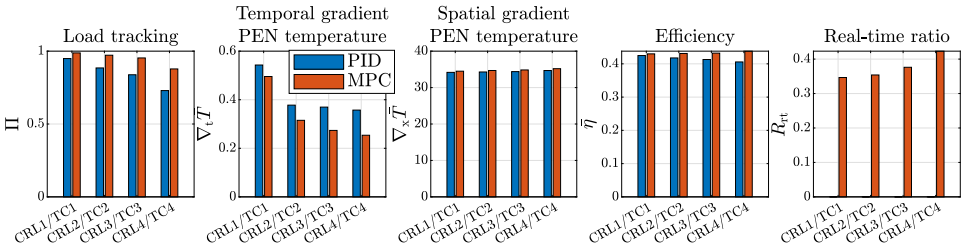

Fig. 11. Performance indicators for simulation scenario 2.

operation closer to the constraint and further improve the power modulation rate of the SOFC. Therefore, it is beneficial to implement a 1D representation of the SOFC in the TC-MPC prediction model. However, this poses challenges since the 1D spatial discretised simulation model in the benchmark system includes 968 states [51]. To enable real-time optimisation, the 1D model must be simplified to reduce the number of states while preserving the spatial distribution of temperature to capture the local behaviour. Furthermore, the prediction horizon of 20 s is sufficient to regulate the temporal temperature gradient dynamics in the SOFC and the output power. However, the temperature dynamics have a much larger timescale (order 100−500 [s]). For any (sub)optimal operation, the prediction horizon should be of a similar order as the slowest dynamics of the system. However, with the current sampling time $t_s = 1$, such a prediction horizon would increase the amount of decision variables beyond the real-time tractable point.

The simulations and the results of this paper do not reflect a particular maritime use case. Therefore, the applicability of the results is not limited to maritime applications but could improve dynamic load-tracking capabilities in many SOFC applications. It is important to examine the specific power profile of a particular vessel type to understand the implications of these improvements in a maritime context. The improvements can be accounted for in the energy management strategy, which impacts the design and operation of the vessel's hybrid power system. However, without a defined power rate-of-change limit for the SOFC system, the TC-MPC should offer feedback on how much dynamic load the SOFC can support. Therefore, alongside assessing the impact of these improvements through the vessel's energy management strategy, the integration of the TC-MPC into the energy management system must also be considered.

7. Conclusion and future work

This work introduces a TC-MPC strategy incorporating thermal stress considerations to determine the maximum rate at which the power of the SOFC benchmark system is regulated. The key findings of this research are as follows:

- During dynamic load changes, the temporal temperature gradient is the critical thermal stress indicator to take into account. The KPI shows that the absolute spatial gradient does not vary for the various rate-of-change constraints. The spatial gradient is closely tied to operating temperature and power, indicating it can be effectively managed by controlling the temperature and preventing overshoot beyond the operating point.
- Both the baseline PID strategy and the TC-MPC show that the maximum local spatial temperature gradient in the SOFC remains unaffected by the power modulation rate-of-change. However, the local temporal temperature gradient in the SOFC increases significantly as the power modulation rate-of-change increases.
- The proposed TC-MPC effectively limits the maximum local temporal temperature gradient in the SOFC while improving the load tracking capabilities for the benchmark system with 1%–17% compared to the baseline PID strategy. This is specific to the generic stand-alone system configuration. However, as the thermal constraints apply to the SOFC, similar improvement trends can be expected for other configurations. The predicted SOFC temperature rate-of-change by the TC-MPC differs from the actual observed local temporal temperature gradient in the 1D SOFC model benchmark system. Therefore, the local temporal temperature gradient in the SOFC is not constrained but only reduced. The local spatial temperature gradient in the SOFC shows no significant difference while operating with the baseline PID or TC-MPC.
- The TC-MPC strategy is computationally tractable with a real-time CPU ratio of 0.44 or less.
- The load tracking improvements are primarily due to the thermal constraints, not just the predictive capabilities of the TC-MPC. While the TC-MPC can respond to load changes earlier than the baseline PID, due to its 20-second prediction horizon, the power modulations in the results are significantly slower than 20 s. Furthermore, the results indicate a steeper output power slope for the TC-MPC strategies than the baseline PID.

In future research, we suggest exploring the impact of the proposed TC-MPC strategy in a maritime context through a dedicated case study. The TC-MPC strategy could be further enhanced by incorporating a 1D discretised SOFC prediction model. However, the current version of the 1D model is not suitable for optimisation and will require

Table A.1
Calculated KPIs for scenario 1: Ramp-down and ramp-up.

Controller:	KPI:									
	Π [-]		$\nabla_t \bar{T}$ [Ks^{-1}]		$\nabla_x \bar{T}$ [Kcm^{-1}]		$\bar{\eta}$ [-]		ϕ_{rt} [-]	
CRL-1/TC-1	0.96	0.97	0.59	0.45	36.8	38.4	0.40	0.40	$4.8{\cdot}10^{-5}$	0.28
CRL-2/TC-2	0.87	0.93	0.37	0.37	37.3	38.3	0.39	0.40	$4.5{\cdot}10^{-5}$	0.34
CRL-3/TC-3	0.80	0.90	0.31	0.32	37.2	38.0	0.39	0.40	$5.3{\cdot}10^{-5}$	0.45
CRL-4/TC-4	0.61	0.78	0.22	0.23	36.7	38.7	0.38	0.40	$4.7{\cdot}10^{-5}$	0.47

Table A.2
Calculated KPIs for scenario 2: Load cycle.

Controller:	KPI:									
	Π [-]		$\nabla_t \bar{T}$ [Ks^{-1}]		$\nabla_x \bar{T}$ [Kcm^{-1}]		$\bar{\eta}$ [-]		ϕ_{rt} [-]	
CRL-1/TC-1	0.93	0.98	0.59	0.50	34.2	34.5	0.57	0.58	$6.1{\cdot}10^{-5}$	0.36
CRL-2/TC-2	0.84	0.96	0.38	0.32	34.3	34.7	0.56	0.58	$5.7{\cdot}10^{-5}$	0.36
CRL-3/TC-3	0.77	0.93	0.37	0.27	34.4	34.8	0.55	0.58	$5.7{\cdot}10^{-5}$	0.39
CRL-4/TC-4	0.67	0.85	0.36	0.28	34.7	35.2	0.54	0.58	$5.8{\cdot}10^{-5}$	0.44

simplification to achieve this. Additionally, extending the prediction horizon beyond 20 s could improve the SOFC operation. SOFC systems are often more complex than the stand-alone system discussed in this research, by incorporating features such as a pre-reformer or anode off-gas recirculation. These additions will increase the complexity of the optimisation problem but also offer greater flexibility in controlling the internal processes of the SOFC, which the TC-MPC could leverage to enhance the load-tracking performance of SOFC systems further. Further validation of the control strategy can be made with Hardware-in-the-loop testing to verify real-time feasibility, robustness to latency and measurement noise. This requires optimising the MPC for embedded control, by code generation and parallelisation of calculations.

CRediT authorship contribution statement

Matthis H. de Lange: Writing – review & editing, Writing – original draft, Validation, Software, Methodology, Investigation, Formal analysis, Conceptualization. **Pablo Segovia:** Writing – review & editing, Supervision, Methodology, Conceptualization. **Rudy R. Negenborn:** Writing – review & editing, Supervision, Methodology, Conceptualization. **Lindert van Biert:** Writing – review & editing, Supervision, Methodology, Conceptualization.

Declaration of competing interest

The authors declare the following financial interests/personal relationships which may be considered as potential competing interests: M.H. de Lange reports financial support was provided by European Commission. If there are other authors, they declare that they have no known competing financial interests or personal relationships that could have appeared to influence the work reported in this paper.

Acknowledgements

The research is supported by the European Consortium ‘HELENUS’ (Grant agreement ID: 1010567). The HELENUS Project aims to demonstrate the applicability, scalability and fuel-flexibility of highly efficient solid oxide fuel cells (SOFCs) in various large ship applications.

Appendix. Calculated KPIs for the simulation scenarios

The KPIs for each simulation scenario are calculated as given in Section 3.4. Table A.1 provides the KPI values for scenario 1: Ramp-down and ramp-up. Table A.2 summarises the KPI values for scenario 2: Load cycle.

Data availability

Data will be made available on request.

References

[1] International Maritime Organization. Fourth IMO GHG study 2020. 2020.
[2] International Maritime Organization. 2023 IMO strategy on reduction of GHG emissions from ships. 2023.
[3] European Commission. European green deal: Agreement reached on cutting maritime transport emissions by promoting sustainable fuels for shipping. 2023.
[4] Lindstad E, Lagemann B, Rialland A, Gamlem GM, Valland A. Reduction of maritime GHG emissions and the potential role of E-fuels. Transp Res Part D: Transp Environ 2021;101:103075.
[5] Wang Z, Dong B, Li M, Ji Y, Han F. Configuration of low-carbon fuels green marine power systems in diverse ship types and applications. Energy Convers Manage 2024;302:118139.
[6] Bouman EA, Lindstad E, Rialland AI, Strømman AH. State-of-the-art technologies, measures, and potential for reducing GHG emissions from shipping–A review. Transp Res Part D: Transp Environ 2017;52:408–21.
[7] Thaler B, Kanchiralla FM, Posch S, Pirker G, Wimmer A, Brynolf S, Wermuth N. Optimal design and operation of maritime energy systems based on renewable methanol and closed carbon cycles. Energy Convers Manage 2022;269:116064.
[8] Rivarolo M, Rattazzi D, Magistri L, Massardo A. Multi-criteria comparison of power generation and fuel storage solutions for maritime application. Energy Convers Manage 2021;244:114506.
[9] Inal OB, Deniz C. Assessment of fuel cell types for ships: Based on multi-criteria decision analysis. J Clean Prod 2020;265:121734.
[10] Xing H, Stuart C, Spence S, Chen H. Fuel cell power systems for maritime applications: Progress and perspectives. Sustainability 2021;13(3):1213.
[11] Xu Q, Guo Z, Xia L, He Q, Li Z, Temitope Bello I, Zheng K, Ni M. A comprehensive review of solid oxide fuel cells operating on various promising alternative fuels. Energy Convers Manage 2022;253:115175.
[12] Li C, Wang Z, Liu H, Guo F, Li C, Xiu X, Wang C, Qin J, Wei L. Energy and configuration management strategy for solid oxide fuel cell/engine/battery hybrid power system with methanol on marine: A case study. Energy Convers Manage 2024;307:118355.
[13] Roux M, Lodato C, Laurent A, Astrup T. A review of life cycle assessment studies of maritime fuels: Critical insights, gaps, and recommendations. Sustain Prod Consum 2024;50:69–86.
[14] van Biert L, Godjevac M, Visser K, Aravind P. A review of fuel cell systems for maritime applications. J Power Sources 2016;327:345–64.
[15] Kistner L, Bensmann A, Hanke-Rauschenbach R. Potentials and limitations of battery-electric container ship propulsion systems. Energy Convers Manag: X 2024;21:100507.
[16] Van Veldhuizen B, Van Biert L, Aravind PV, Visser K. Solid oxide fuel cells for marine applications. Int J Energy Res 2023;2023(1):5163448.
[17] Baldi F, Moret S, Tammi K, Maréchal F. The role of solid oxide fuel cells in future ship energy systems. Energy 2020;194:116811.
[18] Haseltalab A, van Biert L, Sapra H, Mestemaker B, Negenborn RR. Component sizing and energy management for SOFC-based ship power systems. Energy Convers Manage 2021;245:114625.
[19] Kistner L, Bensmann A, Hanke-Rauschenbach R. Optimal design of power gradient limited solid oxide fuel cell systems with hybrid storage support for ship applications. Energy Convers Manage 2021;243:114396.

[20] Mueller F, Jabbari F, Gaynor R, Brouwer J. Novel solid oxide fuel cell system controller for rapid load following. J Power Sources 2007;172(1):308–23.
[21] Hollmann J, Kabelac S. Steady-state and transient operation of solid oxide fuel cell systems with anode off-gas recirculation within a highly constrained operating range. Energies 2023;16(23):7827.
[22] Atkinson A, Selcuk A. Mechanical behaviour of ceramic oxygen ion-conducting membranes. Solid State Ion 2000;134(1–2):59–66.
[23] Heenan TMM, Lu X, Robinson JB, Iacoviello F, Brett DJL, Shearing PR. Thermally driven SOFC degradation in 4D: Part II. Macroscale. J Electrochem Soc 2018;165(11):F932.
[24] Schäfer F, Egger S, Steiner D, Carré M, Eichel R-A. Control of oxygen-to-carbon ratio and fuel utilization with regard to solid oxide fuel cell systems with anode exhaust gas recirculation: A review. J Power Sources 2022;524:231077.
[25] Franklin GF, Powell JD, Emami-Naeini A, Powell JD. In: Feedback Control of Dynamic Systems, vol. 4, Prentice hall Upper Saddle River; 2002.
[26] de Lange M, Segovia P, Negenborn RR, van Biert L. A framework for advanced safety-constraint control of solid oxide fuel cell systems in maritime applications. In: Proceedings of the 16th European SOFC & SOE forum. Lucerne, Switzerland: EFCF; 2024.
[27] Rawlings JB, Mayne DQ, Diehl M, et al. In: Model Predictive Control: Theory, Computation, and Design, vol. 2, Nob Hill Publishing Madison, WI; 2017.
[28] Braun RJ. Optimal Design and Operation of Solid Oxide Fuel Cell Systems for Small-Scale Stationary Applications (Ph.D. thesis), The University of Wisconsin-Madison; 2002.
[29] Chaisantikulwat A, Diaz-Goano C, Meadows ES. Dynamic modelling and control of planar anode-supported solid oxide fuel cell. Comput Chem Eng 2008;32(10):2365–81.
[30] Frenkel W, Kersten J, Husmann R, Aschemann H. Design of robust PID controllers for SOFC stacks. In: Proceedings of the 2022 IEEE conference on control technology and applications. CCTA, Trieste, Italy; 2022, p. 510–5.
[31] Li Y, Shen J, Lu J. Constrained model predictive control of a solid oxide fuel cell based on genetic optimization. J Power Sources 2011;196(14):5873–80.
[32] Carre M, Brandenburger R, Friede W, Lapicque F, Limbeck U, Da Silva P. Feedforward control of a solid oxide fuel cell system with anode offgas recycle. J Power Sources 2015;282:498–510.
[33] Pohjoranta A, Halinen M, Pennanen J, Kiviaho J. Model predictive control of the solid oxide fuel cell stack temperature with models based on experimental data. J Power Sources 2015;277:239–50.
[34] Fardadi M, Mueller F, Jabbari F. Feedback control of solid oxide fuel cell spatial temperature variation. J Power Sources 2010;195(13):4222–33.
[35] Reineh MS, Fardadi M, Jabbari F. Thermal control of SOFC: An anti-windup approach for maximizing usable power. In: Proceedings of the 2017 IEEE conference on control technology and applications. CCTA, Maui, HI, USA; 2017, p. 311–6.
[36] Hajimolana S, Tonekabonimoghadam S, Hussain MA, Chakrabarti M, Jayakumar N, Hashim M. Thermal stress management of a solid oxide fuel cell using neural network predictive control. Energy 2013;62:320–9.
[37] Skogestad S, Postlethwaite I. Multivariable Feedback Control: Analysis and Design. john Wiley & sons; 2005.
[38] Stiller C, Thorud B, Bolland O, Kandepu R, Imsland L. Control strategy for a solid oxide fuel cell and gas turbine hybrid system. J Power Sources 2006;158(1):303–15.
[39] Spivey BJ, Edgar TF. Dynamic modeling, simulation, and MIMO predictive control of a tubular solid oxide fuel cell. J Process Control 2012;22(8):1502–20.
[40] Sanandaji BM, Vincent TL, Colclasure AM, Kee RJ. Modeling and control of tubular solid-oxide fuel cell systems: II. Nonlinear model reduction and model predictive control. J Power Sources 2011;196(1):208–17.
[41] Zhang X, Chan S, Ho HK, Li J, Li G, Feng Z. Nonlinear model predictive control based on the moving horizon state estimation for the solid oxide fuel cell. Int J Hydrog Energy 2008;33(9):2355–66.
[42] Mueller F, Fardadi M, Shaffer B, Brouwer J, Jabbari F. Transient performance of integrated SOFC system including spatial temperature control. In: Proceedings of the international conference on fuel cell science, engineering and technology, vol. 2, Brooklyn, New York, USA; 2010, p. 237–47.
[43] Van Biert L, Godjevac M, Visser K, Aravind P. Dynamic modelling of a direct internal reforming solid oxide fuel cell stack based on single cell experiments. Appl Energy 2019;250:976–90.
[44] Pukrushpan JT, Peng H, Stefanopoulou AG. Control-oriented modeling and analysis for automotive fuel cell systems. J Dyn Syst., Meas Control 2004;126(1):14–25.
[45] Marra D, Pianese C, Polverino P, Sorrentino M. Models for Solid Oxide Fuel Cell Systems. Springer; 2016.
[46] Pukrushpan JT. Modeling and Control of Fuel Cell Systems and Fuel Processors (Ph.D. thesis), University of Michigan; 2003.
[47] Stiller C. Design, Operation and Control Modelling of SOFC/GT Hybrid Systems (Ph.D. thesis), Norwegian University of Science and Technology; 2006.
[48] Mueller F, Brouwer J, Jabbari F, Samuelsen S. Dynamic simulation of an integrated solid oxide fuel cell system including current-based fuel flow control. J Fuel Cell Sci Technol 2005;3(2):144–54.
[49] Kupecki J. Modeling, design, construction, and operation of power generators with solid oxide fuel cells: From single cell to complete power system. Springer; 2018.
[50] Gahinet P, Apkarian P. Structured $\mathcal{H}_\infty$ synthesis in MATLAB. IFAC Proc Vol 2011;44(1):1435–40, 18th IFAC World Congress.
[51] van Biert L, Segovia Castillo P, Haseltalab A, Negenborn RR. A reduced-order model of a solid oxide fuel cell stack for model predictive control. In: Proceedings of the International Ship Control Systems Symposium, vol. 16, 2022, p. 26.
[52] Köhler J, Soloperto R, Müller MA, Allgöwer F. A computationally efficient robust model predictive control framework for uncertain nonlinear systems. IEEE Trans Autom Control 2020;66(2):794–801.
[53] Limon D, Ferramosca A, Alvarado I, Alamo T. Nonlinear MPC for tracking piece-wise constant reference signals. IEEE Trans Autom Control 2018;63(11):3735–50.
[54] Betti G, Farina M, Scattolini R. An MPC algorithm for offset-free tracking of constant reference signals. In: Proceedings of the 2012 IEEE 51st IEEE Conference on Decision and Control. CDC, Maui, HI, USA; 2012, p. 5182–7.
[55] Koelewijn P. Analysis and Control of Nonlinear Systems with Stability and Performance Guarantees: A Linear Parameter-Varying Approach (Ph.D. thesis), Eindhoven University of Technology; 2023.
[56] Berberich J, Köhler J, Müller MA, Allgöwer F. Linear tracking MPC for nonlinear systems—Part I: The model-based case. IEEE Trans Autom Control 2022;67(9):4390–405.
[57] (D) SG. Technical Documentation Integrated Stack Module (ISM), Tech. rep..
[58] Andersson JAE, Gillis J, Horn G, Rawlings JB, Diehl M. CasADi – A software framework for nonlinear optimization and optimal control. Math Program Comput 2019;11(1):1–36.
[59] Pohjoranta A, Halinen M, Pennanen J, Kiviaho J. Solid oxide fuel cell stack temperature estimation with data-based modeling – designed experiments and parameter identification. J Power Sources 2015;277:464–73.
[60] Krishnamoorthy D. On tuning parameterized control policies online for safety-critical systems - applied to biomedical systems. IFAC-PapersOnLine 2023;56(2):5781–6, 22nd IFAC World Congress.